

Chapter 4

Population modelling and computation

In this chapter an overview is presented of a scheme for handling the assembly and solution of collisional-radiative matrices suited to all future collisional-radiative work. In particular it is designed to support studies on heavy species as well as consistent studies involving bound and free states. In this chapter a high quantum shell module is developed which evaluates hydrogenic populations, this will be used to predict all the population distributions necessary for the hydrogen series limit spectral feature code of chapter 5. In section 4.1 the general picture for the new model is outlined. Section 4.2 describes a new set of Gaunt factors for use in the model. The details of the high n-shell collisional-radiative module in the computational implementation are then presented in section 4.3 and in section 4.4 an analysis is done into the validity and automation of the bundling cut-off scheme proposed in the new model.

4.1 An overview of the model

There already exist collisional-radiative codes for light elements within the structure of the ADAS suite of codes (Summers, 2001). These codes have been well tested and are proven to be effective in dealing with light elements. As has been described in chapter 1, it is inappropriate to apply these codes to heavy species and an alternative scheme

n_0	$\gamma\pi J$
n_1	$(\gamma_p\pi_p J_p)nljJ$
n_2	$(\gamma_p\pi_p J_p)nlj$
n_3	$(\gamma_p\pi_p J_p)nl$
n_4	$(\gamma_p\pi_p J_p)n$

Figure 4.1: The details of the bundling scheme proposed for the new model.

must be developed. Figure 4.1 shows the new general picture with the switching principal quantum shells defining the subdivisions. In this new model one considers a fully resolved picture for the low levels, with the valence electron in the core. Here γ represents the configuration, π the parity and J the total angular momentum of the system. If the valence electron is in a more highly excited principal quantum shell it is possible to view the electron as ‘built’ on a parent structure. Here γ_p represents the parent level’s configuration, π_p its parity and J_p its total angular momentum. The decreasing levels of resolution become valid as the levels become more degenerate and level populations become statistically distributed. One is therefore able to bundle the populations progressively into these less resolved pictures.

With the subdivisions in the level schemes shown in figure 4.1 it is possible to modularise the assembly of the collisional-radiative matrix, in particular for transitions where the parent is invariant. Consider briefly how the different levels of resolution that such a model possesses should be dealt with. For transitions within the two lowest schemes (i.e. $n < n_1$), one has a fully J-resolved system with corresponding transitions between all the possible levels. The rates for these regimes must be of high quality due to the detailed spectroscopy that is expected to be performed on the resulting spectra. These rates are assembled from the most comprehensive calculated and measured data available. The treatment of these lower levels falls within

$$N_{(\gamma_p \pi_p J_p)nl} = \frac{(2l+1)}{n^2} N_{(\gamma_p \pi_p J_p)n} \quad (4.2)$$

The rates for these higher states will generally be hydrogenic expressions (or quantum defect theory based extensions of hydrogenic expressions) from a radial matrix element point of view, the main alterations being in the angular parts required to account for the new degrees of resolution and the new coupling pictures that will be used. These angular parts will be incorporated in the Gaunt factors. Thus new Gaunt factor expressions must be derived which allow for transitions between all the necessary levels of resolution (see section 4.2, with results summarised in table 4.1).

4.1.1 Definition of block structures for advanced computation

Before proceeding with the details of the newly proposed code it is useful to review and define more carefully the basic building blocks that will be used and how they carry through to the final collisional-radiative matrix.

Block primitives

As can be seen from (4.1) the most basic matrix building block is that for transitions between two levels of resolution or within a single scheme, such as $nlj \rightarrow nl$, or $nlj \rightarrow nlj$. These building blocks will be referred to as ‘block primitives’ analogous to the ‘feature primitives’ used in the spectral feature generation codes of ADAS 602-604 (Summers, 2001), and in the high series spectral feature generation work of chapter 5. The block primitive represents the foundation upon which all the C-R matrices will be built. The C-R code developed in this chapter is modularised such that each module returns a block primitive for assembly into larger C-R structures.

Blocks

We refer to the assembled structure of block primitives as ‘blocks’, analogous to spectral ‘features’. Thus ADAS 311 run in its hydrogen setup already returns a block for transitions between $nlSL$ and nS states which contains block primitives

for $nlSL \rightarrow n'l'S'L'$, $nlSL \rightarrow n'S'$, $nS \rightarrow n'l'S'L'$ and $nS \rightarrow n'S'$. Note that it is possible to assemble these blocks to obtain larger more general collisional-radiative matrices which allow for complexities such as parent changing transitions.

Superblocks

This assembly of blocks is referred to as a ‘superblock’, and is analogous to the spectral ‘superfeature’. A superblock might typically contain on its diagonal, block partitions in which the parent configuration does not change. The off-diagonal partitions would then contain parent changing blocks. The superblock matrix would then be solved to obtain a comprehensive population solution for the atomic system under consideration.

Description of the particular block structure for the new model

The final aim of the new model is the assembly of such a superblock. The first diagonal block will contain all the transitions within the $(\gamma\pi J)$ scheme, where there is no defined parent. The next set of diagonal blocks describe non-parent changing transitions within the $(\gamma_p\pi_p J_p)nljJ$ scheme, with the off-diagonal blocks accounting for parent changing transition within this scheme and transitions down to $(\gamma\pi J)$. As has been noted, these blocks will be assembled using the existing ADAS 208 approach. The higher diagonal elements are then blocks for non-parent changing transitions within the remaining three resolution schemes, that is blocks of the form

$$\begin{bmatrix} C_{(P)nlj \rightarrow (P)nlj} & C_{(P)nlj \rightarrow (P)nl} & C_{(P)nlj \rightarrow (P)n} \\ C_{(P)nl \rightarrow (P)nlj} & C_{(P)nl \rightarrow (P)nl} & C_{(P)nl \rightarrow (P)n} \\ C_{(P)n \rightarrow (P)nlj} & C_{(P)n \rightarrow (P)nl} & C_{(P)n \rightarrow (P)n} \end{bmatrix} \quad (4.3)$$

The neighbouring off-diagonal blocks are for parent changing transitions within these three schemes. They are negligible contributors to the population structure, allowing them to be set to zero. There only remains the first few horizontal and vertical strips accounting for transitions from the upper three schemes to the lower two. These are

filled in using the projection scheme, as already used in ADAS 208.

4.2 Gaunt factors revisited

4.2.1 Background

For this work new Gaunt factors were developed accounting for all the possible coupling schemes for the initial and final states. Gaunt factors are essentially quantum mechanical corrections on classically derived oscillator strengths. The original Gaunt factors for b-b, b-f and f-f transitions were put together in Menzel & Pekeris (1935). Efficient methods have been developed for their determination (Burgess & Summers, 1987). It is usual to evaluate the radial and angular components of the Gaunt factor separately. The bound-bound Gaunt factor is described by

$$g_{i,i'}^I(\nu, \nu') = \frac{\sqrt{3}}{\pi 2^4} \left(\frac{E - E'}{z_1^2 I_H} \right)^4 \frac{1}{\omega_\gamma} Q_{i,i'} R_{i,i'}^I(\nu, \nu') \quad (4.4)$$

where ω_γ is the statistical weight of the parent state, R is the radial integral component and Q contains the angular factors. Q and R can also be expressed as

$$Q_{i,i'} R_{i,i'}^I(\nu, \nu') = \langle (S_P L_P J_P M_P) n l j m J M | \underline{r} | (S'_P L'_P J'_P M'_P) n' l' j' m' J' M' \rangle \quad (4.5)$$

The evaluation of this expression allows immediate calculation of the corresponding Gaunt factor via equation (4.4). Thus the evaluation of equation (4.5) represents the main body of work involved in the calculation of the new Gaunt factors. The bound-free and free-free Gaunt factors can be evaluated by analytically extending the bound-bound expression to free states, as in the continuity work of chapter 3.

4.2.2 Gaunt factor evaluated for j-j coupling

Consider a transition between two fully J-resolved levels, we evaluate the $Q_{i,i'} R_{i,i'}^I(\nu, \nu')$ component of the Gaunt factor and split the position vector \underline{r} into its radial and spherical harmonic components. The expression that needs to be evaluated becomes

$$\begin{aligned} & \langle (S_P L_P J_P) n l j J M | \underline{r} | (S'_P L'_P J'_P) n' l' j' J' M' \rangle = \\ & \langle (S_P L_P J_P) n l j J M | r Y_{1\mu} | (S'_P L'_P J'_P) n' l' j' J' M' \rangle \end{aligned} \quad (4.6)$$

In evaluating this equation, a similar technique to the one used in the L-S coupled Gaunt factor work of Burgess & Summers (1987) is used. From appendix-A the final result is

$$\begin{aligned} & | \langle (S_P L_P J_P) n l j J | r Y_1 | (S'_P L'_P J'_P) n' l' j' J' \rangle |^2 \\ & = (2J+1)(2j+1)(2j'+1)(2J'+1) \delta(S_P L_P J_P; S'_P L'_P J'_P) \\ & \quad \times | \langle n l | r | n' l' \rangle |^2 | \langle l | Y_1 | l' \rangle |^2 \left\{ \begin{matrix} j & J & J_P \\ J' & j' & 1 \end{matrix} \right\}^2 \left\{ \begin{matrix} j' & l' & 1/2 \\ l & j & 1 \end{matrix} \right\}^2 \end{aligned} \quad (4.7)$$

Table 4.1 shows the results of this expression for various levels of bundling resolution. The tabulated values can then be used to evaluate $Q_{i,i'} R_{i,i'}^I(\nu, \nu')$, thus Gaunt factors for j-j coupled to j-j coupled levels can be calculated.

4.2.3 Cross coupling Gaunt factors evaluated

Consider a transition in which a j-j coupled level goes to an L-S coupled level or vice-versa. As the very low level treatment for the future heavy ion work may be done in an L-S coupling framework it is necessary to develop Gaunt factors that allow for these cross-coupling transitions. The method of solution follows closely with that for the j-j coupling to j-j coupling picture from the previous section, this time the expression to be evaluated is:

$$| \langle (S_P L_P) n l S L J | r Y_1 | (S'_P L'_P J'_P) n' l' j' J' \rangle |^2 \quad (4.8)$$

From appendix A this reduces to

$$= (2J+1)(2J'+1)(2S+1)(2L+1)(2j'+1)^2(2J'_P+1)$$

	$(S_P L_P J_P) n l j j'$	$(S_P L_P J_P) n l' j' j'$	$(S_P L_P J_P) n l' j' j'$	$(S_P L_P J_P) n l' l'$	$(S_P L_P J_P) n l'$
$(S_P L_P J_P) n l j J$	$(2J+1)(2J'+1)(2j+1)(2j'+1)$ $\left\{ \begin{matrix} j & J & J_P \\ j' & j' & 1 \end{matrix} \right\}^2$ $\left\{ \begin{matrix} j' & l' & 1/2 \\ l & j & 1 \end{matrix} \right\}^2$ $ \langle l \ Y_1 \ l' \rangle > ^2 \langle n l r n l' \rangle > ^2$	$(2J+1)(2j'+1)$ $\left\{ \begin{matrix} j' & l' & 1/2 \\ l & j & 1 \end{matrix} \right\}^2$ $ \langle l \ Y_1 \ l' \rangle > ^2 \langle n l r n l' \rangle > ^2$	$(2J+1)(2j'+1)$ $\left\{ \begin{matrix} j' & l' & 1/2 \\ l & j & 1 \end{matrix} \right\}^2$ $ \langle l \ Y_1 \ l' \rangle > ^2 \langle n l r n l' \rangle > ^2$	$\frac{(2J+1)}{(2l+1)}$ $ \langle l \ Y_1 \ l' \rangle > ^2 \langle n l r n l' \rangle > ^2$	$\frac{(2J+1)}{(2l+1)}$ $\sum_{l'} \langle l \ Y_1 \ l' \rangle > ^2 \langle n l r n l' \rangle > ^2$
$(S_P L_P J_P) n l j$	$(2J'+1)(2j+1)$ $\left\{ \begin{matrix} j' & l' & 1/2 \\ l & j & 1 \end{matrix} \right\}^2$ $ \langle l \ Y_1 \ l' \rangle > ^2 \langle n l r n l' \rangle > ^2$	$(2j'+1)(2J_P+1)(2j+1)$ $\left\{ \begin{matrix} j' & l' & 1/2 \\ l & j & 1 \end{matrix} \right\}^2$ $ \langle l \ Y_1 \ l' \rangle > ^2 \langle n l r n l' \rangle > ^2$	$(2j'+1)(2J_P+1)(2j+1)$ $\left\{ \begin{matrix} j' & l' & 1/2 \\ l & j & 1 \end{matrix} \right\}^2$ $ \langle l \ Y_1 \ l' \rangle > ^2 \langle n l r n l' \rangle > ^2$	$\frac{(2J_P+1)(2j+1)}{(2l+1)}$ $ \langle l \ Y_1 \ l' \rangle > ^2 \langle n l r n l' \rangle > ^2$	$\frac{(2J_P+1)(2j+1)}{(2l+1)}$ $\sum_{l'} \langle l \ Y_1 \ l' \rangle > ^2 \langle n l r n l' \rangle > ^2$
$(S_P L_P J_P) n l$	$\frac{(2J'+1)}{(2l+1)}$ $ \langle l \ Y_1 \ l' \rangle > ^2 \langle n l r n l' \rangle > ^2$	$\frac{(2j'+1)(2J_P+1)}{(2l'+1)}$ $ \langle l \ Y_1 \ l' \rangle > ^2 \langle n l r n l' \rangle > ^2$	$\frac{(2j'+1)(2J_P+1)}{(2l'+1)}$ $ \langle l \ Y_1 \ l' \rangle > ^2 \langle n l r n l' \rangle > ^2$	$2(2J_P+1)$ $ \langle l \ Y_1 \ l' \rangle > ^2 \langle n l r n l' \rangle > ^2$	$2(2J_P+1)$ $\sum_{l'} \langle l \ Y_1 \ l' \rangle > ^2 \langle n l r n l' \rangle > ^2$
$(S_P L_P J_P) n$	$\frac{(2J'+1)}{(2l'+1)}$ $\sum_l \langle l \ Y_1 \ l' \rangle > ^2 \langle n l r n l' \rangle > ^2$	$\frac{(2j'+1)(2J_P+1)}{(2l'+1)}$ $\sum_l \langle l \ Y_1 \ l' \rangle > ^2 \langle n l r n l' \rangle > ^2$	$\frac{(2j'+1)(2J_P+1)}{(2l'+1)}$ $\sum_l \langle l \ Y_1 \ l' \rangle > ^2 \langle n l r n l' \rangle > ^2$	$(2J_P+1)$ $\sum_l \langle l \ Y_1 \ l' \rangle > ^2 \langle n l r n l' \rangle > ^2$	$(2J_P+1)$ $\sum_{l'} \langle l \ Y_1 \ l' \rangle > ^2 \langle n l r n l' \rangle > ^2$

Table 4.1: $(j-j)$ coupling to $(j'-j')$ coupling Q and R values evaluated for various levels of resolution.

$$\begin{aligned}
& \times \Sigma_x (2x + 1) (-1)^{3x} \left\{ \begin{array}{ccc} L & l & L_P \\ x & S & J \end{array} \right\}^2 \left\{ \begin{array}{ccc} 1 & l' & l \\ x & J & J' \end{array} \right\}^2 \\
& \times \left\{ \begin{array}{ccc} J'_P & x & 1/2 \\ l' & j' & J' \end{array} \right\}^2 \left\{ \begin{array}{ccc} J'_P & 1/2 & x \\ S & L_P & S_P \end{array} \right\}^2 \\
& \times | \langle nl|r|n'l' \rangle |^2 | \langle l||Y_1||l' \rangle |^2
\end{aligned} \tag{4.9}$$

As before this can be averaged to account for any desired degree of resolution.

4.3 The new collisional-radiative code

We now seek to produce a subroutine that outputs a C-R matrix for non-parent changing transitions that can be called recursively to assemble the superblock described earlier. This is done for nl and n levels of resolution and the method is tested for nlj levels.

4.3.1 nl and n resolution

For the highly excited states one has an n or nl electron on top of a J -resolved core. This is similar to the existing hydrogen mode of ADAS 311 (Summers, 2001) which assembles rates for an nl or n electron on top of a bare nucleus, solving for the populations.

To adapt the code for our purposes the parent statistical weight expression was modified to account for a J -resolved core. The code was modularised such that it returns the block primitives individually. One complication was that ADAS 311 evaluates the nearly degenerate transition rate matrix elements outside the row and column loops. It needs to do this because it uses rates from elsewhere in the matrix to evaluate the lifetimes of the levels involved in the degenerate calculations. In the new code the nearly degenerate rates are evaluated within the row and column loops, the lifetimes being estimated from the level radiative rates evaluated using hydrogenic expressions. When the code is applied to heavy species the lifetimes can be estimated from the initial autostructure run which sets up the energy level structure.

The completed hydrogen module of the code can be run for a user defined set of electron temperatures and densities. Some illustrative results are shown in figure 4.2. It was found that the new modular version of the code agreed with the previous hydrogen results from ADAS 311, and that the population results varied as expected when non-zero J_p values were used. That is, the b-factors are unaltered and the actual population values are reduced by a factor of $(2J_p + 1)$.

4.3.2 *nlj* resolution

A test module was constructed for the *nlj* part of the new code. Consider the bundled-*nl* and bundled-*n* module of the code and split one single *n* level into its *nlj* substates. The population of these *nlj* substates are then solved including all the transition rates between the *nlj* substates and those to and from the surrounding *nl* and *n* states. The hydrogen module of the code is used in a prior calculation to evaluate the surrounding populations and new rate expressions used to evaluate the connecting rates to and from the *nlj* substates. In this way the population distribution within an *nlj* set of levels can be isolated and the *nlj* resolved rates examined. The advantage of generating such a test module before developing a new block primitive code is that one does not need to wait until the whole block primitive module is complete before being able to test it. As future modules are added onto the collisional-radiative code it will become progressively more difficult to error check the contributions from each block primitive. There is a further point from the test module, the *nlj* populations for a single *n* shell can be used to generate a spectral emission profile which will show the distortion produced by the relative populations of the *nlj* sublevels and their relative energy shifts. This is an important connection with our line profile studies and is demonstrated later in this section.

Turning to the details of the test code for a whole block primitive, a perturbative type of approach is done in which from the general C-R matrix block the *nl* block primitive which is to be later expanded into *nlj* sublevels is selected. One has

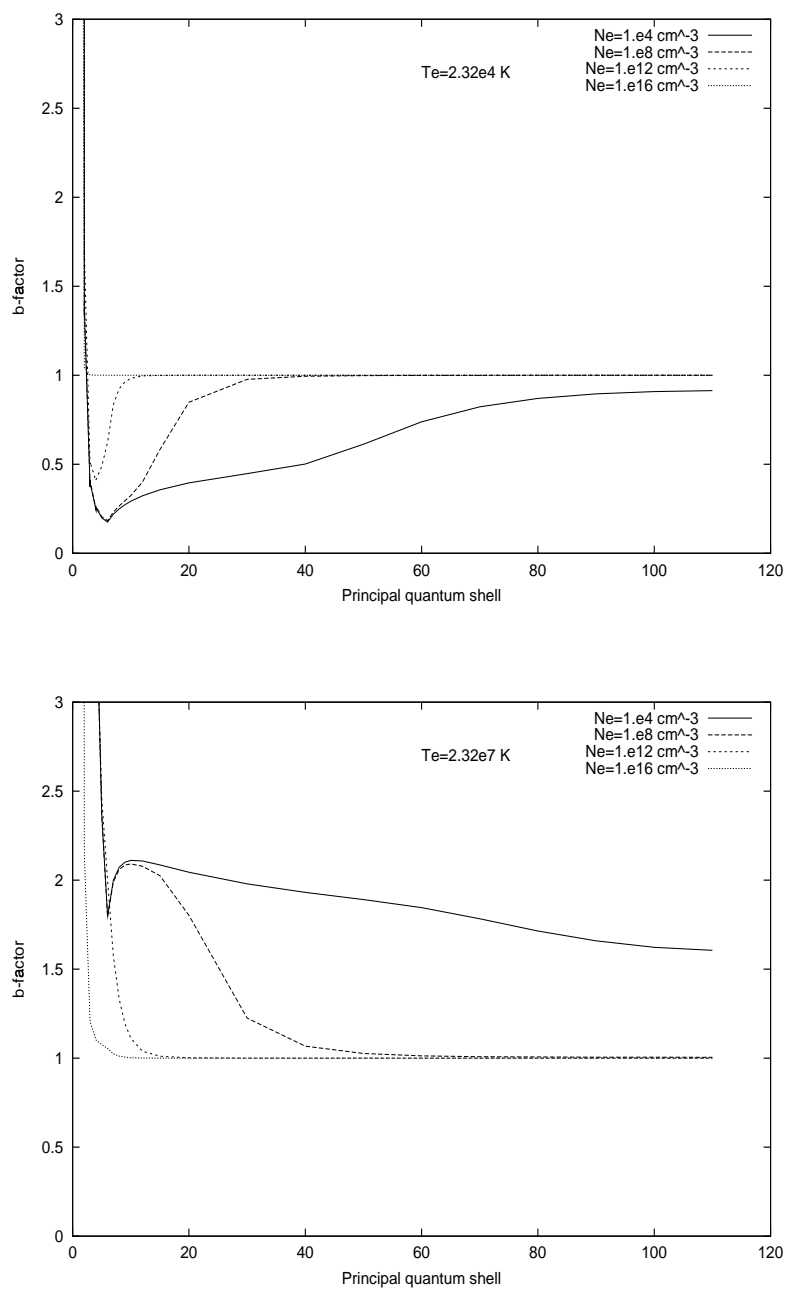


Figure 4.2: Population results from the hydrogen module of the new C-R code.

$$\begin{bmatrix}
\text{low block} & \rightarrow & \rightarrow \\
\leftarrow & \text{chosen} & \rightarrow \\
& \text{nl block} & \\
\leftarrow & \leftarrow & \text{n block}
\end{bmatrix}
\begin{bmatrix}
N_1 \\
\vdots \\
\vdots \\
\vdots \\
\vdots \\
N_{max}
\end{bmatrix}
=
\begin{bmatrix}
RHS \\
\vdots \\
\vdots \\
\vdots \\
\vdots
\end{bmatrix}
\quad (4.10)$$

The existing code solves the matrix equation in a b-factor picture where various atomic constants have been taken out from both the rate expressions and the atomic populations, giving

$$const \times
\begin{bmatrix}
C_{i,k'} & C_{i,n'l'} & C_{i,\bar{n}'} \\
C_{nl,k'} & C_{nl,n'l'} & C_{nl,\bar{n}'} \\
C_{\bar{n},k'} & C_{\bar{n},n'l'} & C_{\bar{n},\bar{n}'}
\end{bmatrix}
\begin{bmatrix}
b_{k'} \\
b_{n'l'} \\
b_{\bar{n}'}
\end{bmatrix}
=
\begin{bmatrix}
RHS_k \\
RHS_{nl} \\
RHS_{\bar{n}}
\end{bmatrix}
\quad (4.11)$$

The test code obtains the solution for the b-factors of this equation. That is,

$$\begin{bmatrix}
b_{k'} \\
b_{n'l'} \\
b_{\bar{n}'}
\end{bmatrix}
=
\frac{1}{const} \times
\begin{bmatrix}
C_{i,k'} & C_{i,n'l'} & C_{i,\bar{n}'} \\
C_{nl,k'} & C_{nl,n'l'} & C_{nl,\bar{n}'} \\
C_{\bar{n},k'} & C_{\bar{n},n'l'} & C_{\bar{n},\bar{n}'}
\end{bmatrix}^{-1}
\begin{bmatrix}
RHS_k \\
RHS_{nl} \\
RHS_{\bar{n}}
\end{bmatrix}
\quad (4.12)$$

One can take equation (4.11) and re-arrange it to isolate the selected nl block primitive. This is performed as follows:

$$[C_{nl,k'}] [b_{k'}] + [C_{nl,n'l'}] [b_{n'l'}] + [C_{nl,\bar{n}'}] [b_{\bar{n}'}] = \frac{1}{const} [RHS_{nl}]
\quad (4.13)$$

$$\begin{aligned}
[C_{nl,n'l'}] [b_{n'l'}] &= \frac{1}{const} [RHS_{nl}] - [C_{nl,k'}] [b_{k'}] - [C_{nl,\bar{n}'}] [b_{\bar{n}'}] \\
&= [new RHS_{nl}]
\end{aligned}
\quad (4.14)$$

We treat this as a new set of equations to solve for the $b_{n'l'}$ on the left hand side, the right hand side being known from the previous solution. The reorganisation can be checked by showing that the $b_{n'l'}$ results agree with their prior values.

The next step is to open up the nl block primitive into its nlj sublevels. Thus one splits each RHS_{nl} into $RHS_{nl-1/2}$ and $RHS_{nl+1/2}$. Similarly each b_{nl} is split into $b_{nl-1/2}$ and $b_{nl+1/2}$.

$$\begin{bmatrix} C_{nlj,n'l'j'} & \dots & \dots & \dots \\ \dots & \dots & \dots & \dots \\ \dots & \dots & \dots & \dots \\ \dots & \dots & \dots & \dots \end{bmatrix} \begin{bmatrix} b_{nlj} \\ \dots \\ \dots \\ \dots \end{bmatrix} = \begin{bmatrix} RHS_{nlj} \\ \dots \\ \dots \\ \dots \end{bmatrix} \quad (4.15)$$

To expand the RHS for nlj resolution it is assumed that these overall rates involving the other n and nl states contribute to the nlj populations statistically. That is

$$RHS_{nl-1/2} = \left(\frac{l}{2l+1} \right) RHS_{nl} \quad (4.16)$$

$$RHS_{nl+1/2} = \left(\frac{l+1}{2l+1} \right) RHS_{nl} \quad (4.17)$$

A similar splitting is assumed (as a first step) for the collisional rates on the left hand side. This is justified as follows: The left hand side is made up of b-factors and rates such as spontaneous emission rates, collisional rates etc. The combination of the statistical weight in the b-factors and in the rate expression means that the collisional rates on the left hand side vary in the same way as the line strengths would. The corresponding weight terms have already been worked out in the previously evaluated Gaunt factor work. From the Gaunt factor tables, the weighting term is

$$\begin{aligned} & \frac{1}{2(2J_p+1)} (2j'+1)(2J_p+1)(2j+1) \left\{ \begin{matrix} j' & l' & 1/2 \\ l & j & 1 \end{matrix} \right\}^2 \\ & = \frac{1}{2} (2j+1)(2j'+1) \left\{ \begin{matrix} j' & l' & 1/2 \\ l & j & 1 \end{matrix} \right\}^2 \end{aligned} \quad (4.18)$$

At this point the equations can again be solved and the results should agree with $b_{n'l'l'-1/2} = b_{n'l'l'+1/2} = b_{n'l'l'}$. After this further check, we can proceed to include the proper rate expressions on the left hand side and evaluate the b-values for the new

nlj module (again assuming knowledge of the right hand side b_n and b_{nl} values). This test module can be used to examine the rate expressions and check limiting cases. In particular the condensation of the module by choosing representative levels can be investigated.

For the test code written here only one single n' is considered such that a distorted $n' \rightarrow n$ spectral transition can be modelled. This code is designed to be a proof that the redistributive rates can be used in the new nlj block primitive. Upon verification of this smaller test module the larger block primitive test code will be written.

So proceeding with the algebra for the smaller test module one returns to equation (4.14) and writes it out more fully in terms of all the possible n values that can appear in the nl partition. That is,

$$\begin{bmatrix} C_{n_0l_0,n_0l_0} & C_{n_0l_0,n_0+1l_1} & \dots & \dots \\ C_{n_0+1l_1,n_0l_0} & C_{n_0+1l_1,n_0+1l_1} & \dots & \dots \\ \dots & \dots & C_{n_{cl_c},n_{cl_c}} & \dots \\ \dots & \dots & \dots & \dots \end{bmatrix} \begin{bmatrix} b_{n_0l_0} \\ b_{n_0+1l_1} \\ b_{n_{cl_c}} \\ \dots \end{bmatrix} = \begin{bmatrix} \text{new RHS} \\ \dots \\ \dots \\ \dots \end{bmatrix} \quad (4.19)$$

Where n_{cl_c} represents the n-shell and corresponding l states that are to be expanded upon into nlj sub-states. Isolating the redistributive rates one is left with:

$$\begin{aligned} [C_{n_{cl_c},n_{cl_c}}] [b_{n_{cl_c}}] &= [RHS_{n_{cl_c}}] - [C_{n_{cl_c},n_0l_0}] [b_{n_0l_0}] - [C_{n_{cl_c},n_0+1l_1}] [b_{n_0+1l_1}] - \dots \\ &= [\text{new RHS}_{n_{cl_c}}] \end{aligned}$$

The procedure continues as described for a whole test block primitive. Results for $n_c = 3$ are shown here. Consider the redistributive rates. Only dipole transitions which redistribute the electrons in j are significant. There are of course ion quadrupole transition that provide J changing transition but as these are within a given nlj group they do not alter the individual j populations. Thus the main mechanism of indirect J redistribution and hence j redistribution is by transfer from $nljJ$ to $nl \pm 1j'J'$. Note that because of the near degeneracy in the relativistic picture of $nl(l+1/2)$ and $nl+1(l-1/2)$, it is only the collisional rates between $nl(l+1/2)J$ and $nl+1(l-1/2)J'$

which matter. These are allowed dipole transitions induced by positive ion impact. A code based on the theory of Pengelly & Seaton (1964) can be used to evaluate the ion collisional transition rates between adjacent l states. For an energy level separation greater than that for which the Pengelly/Seaton approach is valid, an impact parameter code (Burgess & Summers, 1976) can be used. These codes are also used in section 4.4 to evaluate bundling cut-offs.

The b_{nlj} factors evaluated for $z_0 = 36$ and $T_e = 1.05 \times 10^8 K$ (reduced temperature $T_e = 1 \times 10^5 K$) are shown as a function of density (N_e assumed equal to N_i) in figure 4.3. Note that at low densities coronal conditions apply and the populations are determined by spontaneous emission and collisional excitation from the ground. At about $1 \times 10^{22} cm^{-3}$ the j -redistributive rates become significant and couple the nearly degenerate $j = l \pm 1/2$ members of adjacent l s together. Note that the rise in the b -factors is due to population from the $n=2$ shell becoming significant. This was confirmed using ADAS 216. As the density increases further one would hope to see the b_{nl} -factors converging and then the b_n -factors converging. For the example shown in figure 4.3 the behaviour at higher densities is controlled by the n -shell behaviour and it was not possible to isolate the l convergence. Nevertheless the influence of the j -redistributive rates is as expected.

Distorted profiles

With the nlj non-statistical population results a distorted profile can be produced. Firstly a stick plot of the b_{nlj} factors is generated. This is then broadened using a standard Doppler profile expression to produce a distorted profile for a given $n_{upper} \rightarrow n_{lower}$ transition. Note that if the absolute populations are used along with calculated A -values and broadened profiles, an expected emission profile can be produced. We show the b -factor results here to isolate the population and energy scaling behaviour. Figure 4.4 shows a set of calculations for the $n = 3 \rightarrow 2$ transition. The plots are for a scaled density of $1 \times 10^{14} cm^{-3}$ and a scaled temperature of $1 \times 10^7 K$. Note that the energy splitting increases with z_0 , resulting in a distortion of the spectral envelope. The resultant profile is normalised to one. The higher temperature than that used for figure 4.3 produces the increased b -factor values.

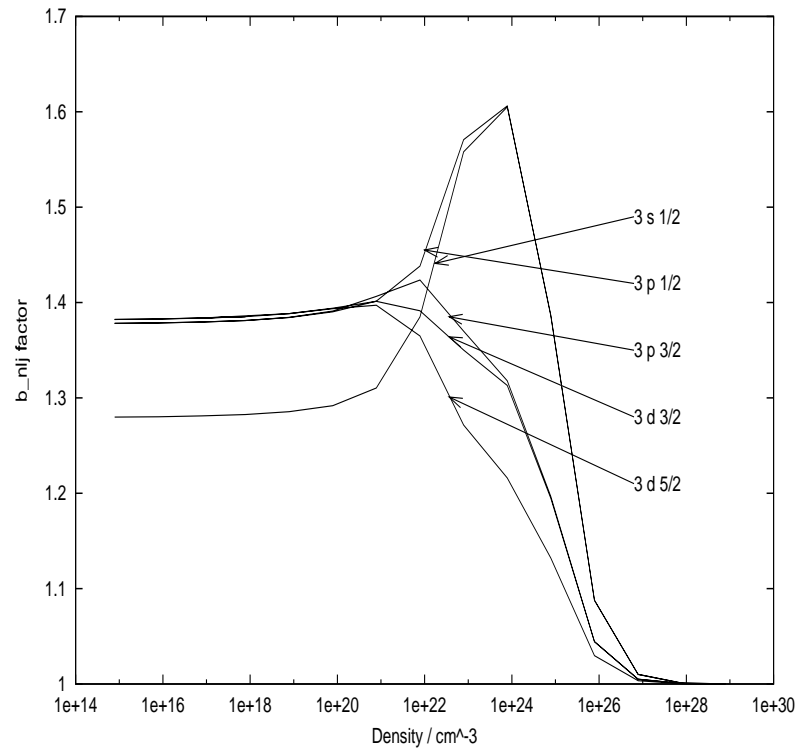


Figure 4.3: b_{nlj} results for $n=3$ as a function of density for $z_0 = 36$ and $T_e = 1.05 \times 10^8 K$.

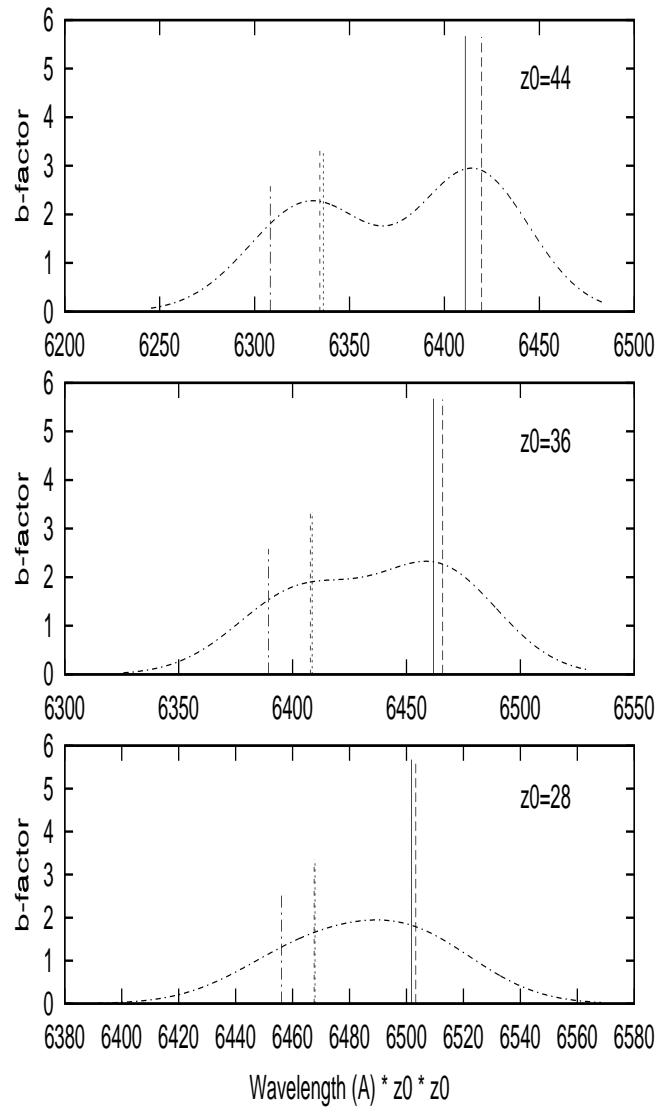


Figure 4.4: Plot showing the fine structure nlj splitting in the $n = 3 \rightarrow 2$ transition. The x-axis is the wavelength $\times z_0^2$ allowing the results for various z_0 s to be plotted on the same scale. The plots are for $z_0 = 28, 36$ & 44 , a reduced temperature of $1 \times 10^7 K$ and a reduced density of $1 \times 10^{14} cm^{-3}$.

4.4 Automatic detection of the bundling cut-offs

It is advantageous if the new collisional-radiative code can automatically detect the bundling cut-offs and set them appropriately. In this section the criteria for such cut-offs for the new collisional-radiative model are determined. The problem is firstly examined from an energy level perspective and then from a rate point of view.

The first step in the heavy species code is an autostructure run to determine the energy level structure. This section shows how typical autostructure data can be used in this general scheme to determine the critical n-shells between bundling regimes. Consider once more the bundling scheme of equation (4.2). It must be determined if there is indeed valid population separation in nl space of the intervals $n_0 < n \leq n_1$ and $n_1 < n \leq n_2$ for bundling to be appropriate. Consider this firstly from the energy level point of view.

4.4.1 Energy level investigation

The relativistic separations of the valence electron fine structure levels from the nl centroid, taken from Condon & Shortley (1935), are given by

$$\begin{aligned}\Delta E_{nl_{l+1/2}} &= \frac{z_1^4 \alpha^2 R_\infty}{n^4} \left(\frac{n}{(l+1)} - \frac{n}{(l+1/2)} \right) \\ \Delta E_{nl_{l-1/2}} &= \frac{z_1^4 \alpha^2 R_\infty}{n^4} \left(\frac{n}{l} - \frac{n}{(l+1/2)} \right)\end{aligned}\quad (4.20)$$

where z_1 is the ion charge $+1$, α is the fine structure constant and R_∞ is the Rydberg energy unit. By contrast, the J separation arises from the electrostatic interaction of the valence electron with the parent core. The interaction is diagonal in J with the level separations from the $(J_p)nlj$ centroid expressible in the form

$$\begin{aligned}\Delta E_{nl_j J} &= \sum_i (f_{2i} F_{2i} + g_{2i} G_{2i}) \\ &= \frac{z_1 R_\infty}{n^3} \sum_i (f_{2i} \bar{F}_{2i} + g_{2i} \bar{G}_{2i})\end{aligned}\quad (4.21)$$

where the “barred” quantities are weakly dependent on z_1 and n and the f s, \bar{F} s and \bar{G} s are of order unity. The \bar{F} s and \bar{G} s are the usual Slater integrals.

Consider a critical energy splitting ΔE_c which is the minimum level separation required for two levels to be resolved. This critical energy separation is determined from the ion collision rates and is the minimum energy separation required for ion collisions to statistically populate the energy levels for the temperature and density of interest. Thus a critical n-shell n_2 will occur above which j levels are statistically populated. Similarly there will be a critical n-shell n_1 above which the J levels are statistically populated. For the proposed bundling to be appropriate we require $n_2 > n_1$. Taking the ratio of equation (4.20) to (4.21) one can see that this separation of bundling intervals $n_0 < n \leq n_1$ and $n_1 < n \leq n_2$ is appropriate if

$$\frac{n_2}{n_1} \sim z_1 \alpha^{2/3} > 1 \quad (4.22)$$

Energy scaling example - Carbon-like isoelectronic sequence

An illustration of the energy level scaling for the Carbon-like sequence is shown below. The superstructure code (Eissner et al., 1974) was used to generate an energy level structure for the C-like sequence with a valence electron that could be placed in a range of n and l shells. The core configuration was held constant at $1s^2 2s^2 2p$ and the Rydberg electron added on top of this configuration. The core configuration thus generated two possible parent states, namely $^2P_{1/2}$ and $^2P_{3/2}$. The energy splitting between these states is expected to be significantly stronger than the j or J fine structure splitting and should scale as z_1^4/n^3 . For each parent configuration we have the further splitting into two possible j states with $j = l + 1/2$ or $j = l - 1/2$, since there is only one outer electron to form the l and s quantum numbers to give us the resultant j for the valence electron. This energy level splitting is expected to scale as in equation (4.20). There exists a further possible energy splitting due to the total J quantum number and this should scale as in equation (4.21). For our C-like sequence we have the following possible total J quantum numbers.

Parent	n	l	j	J			
${}^2P_{1/2}$	n	l	$l - 1/2$	l	$l - 1$		
${}^2P_{1/2}$	n	l	$l + 1/2$	$l + 1$	l		
${}^2P_{3/2}$	n	l	$l - 1/2$	$l + 1$	l	$l - 1$	$l - 2$
${}^2P_{3/2}$	n	l	$l + 1/2$	$l + 2$	$l + 1$	l	$l - 1$

It is expected that the largest energy splitting will be between parent states, followed by the j splitting and then the J separation. If everything scales as expected then it will be possible to predict the bundling cut-offs and assemble the collisional-radiative matrix elements as intended.

Three superstructure runs were performed in order to verify the energy scaling. For all runs the option was used to specify a core configuration and add on a Rydberg electron. The code returned the energy level values in Rydberg units with respect to the lowest level defined. Only a single core configuration was specified in order to isolate the various energy splittings. The first run was performed using a 5f Rydberg electron and z_1 was varied from 1 to 85. For the second run z_1 was held constant at 67 to allow sufficient resolution of the splitting to be generated and n varied from 4 to 16. Lastly with $z_1 = 72$ and $n = 13$, l was varied from 2 through to 10. It was possible from these runs to verify the z_1 , n and l behaviour of the resolved energy level splittings as defined in equations (4.20) and (4.21). Note that it is this scaling behaviour that is sought here, not the evaluation of exact energy level values, hence there is no need for a more complex atomic structure to be entered into the superstructure code.

Considering first the parent energy level splitting. In figures 4.5 - 4.6 we show the z_1 and n behaviour of the parent splitting. The z_1 scaling is as expected i.e. z_1^4 for high z_1 . As for the n -dependence, the parent energy splitting initially falls off sharply with n and then remains constant. It should be noted that the magnitude of the parent splitting is significantly greater than either the j or J splitting (compare the absolute energy difference values of figure 4.5 with those of figures 4.7 - 4.18).

The behaviour of the E_{nlj} fine structure level from the E_{nl} centroid, i.e. equation (4.20) was then investigated. Taking the results from the z_1 run it can be seen from figure 4.7 that the splitting varies as z_1^4 for all possible j values. As for the

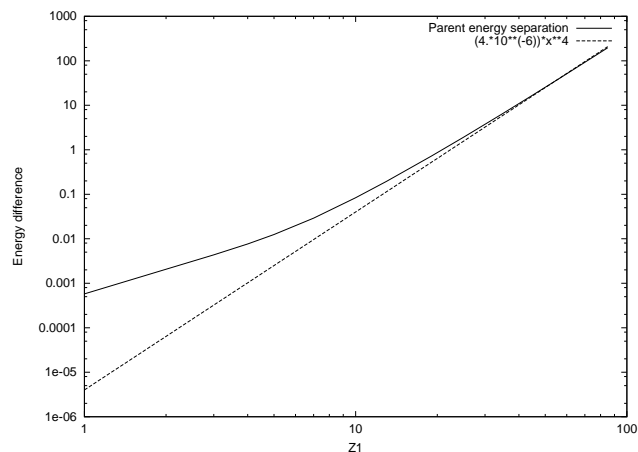


Figure 4.5: $E_2 P_{1/2}$ separation from $E_2 P_{3/1}$ centroid - z_1 dependence. Note that the energy splitting varies as z_1^4 for high z_1 as expected.

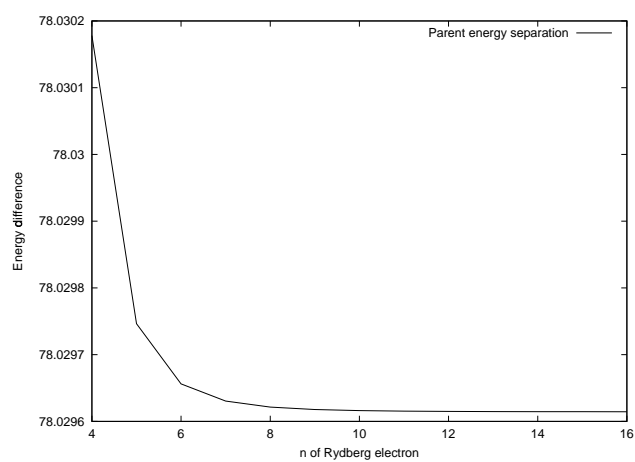


Figure 4.6: $E_2 P_{1/2}$ separation from $E_2 P_{3/1}$ centroid - n dependence.

n-dependence it can be seen in figure 4.8 that for both parents the splitting scales as $1/n^3$. The l-dependence is shown in figures 4.9 - 4.10. It can be seen that the splitting does indeed vary exactly as predicted in equation (4.20), note in particular that the constant of proportionality is also as expected.

Consider next the E_{nljJ} splitting from the E_{nlj} centroid as predicted by equation (4.21). Taking first the z_1 -dependence one can see from figures 4.11 - 4.13 that the energy differences are indeed linear with z_1 . The n-dependence is shown in figures 4.14 - 4.16 and is seen to scale as $1/n^3$.

The l behaviour is not so straightforward, the energy difference splits into two main groups defined by the $j = l - 1/2$ and $j = l + 1/2$ states (see figures 4.17 - 4.18). For low l there is a high degree of variance in the ΔE_{nljJ} behaviour, as expected due to the penetration of these orbitals into the core. As one increases to higher l the behaviour becomes smooth, scaling approximately as $1/l^3$ for the case of the ${}^2P_{3/2}$ parent. In both cases the splitting clearly falls off with increasing l.

From this worked example it can be seen that expressions (4.20) and (4.21) are indeed valid. Thus it is also possible to assess the n_2/n_1 ratio shown in equation (4.22) for the C-like case. Figures 4.19 - 4.22 show the ratio of ΔE_{nljJ} to ΔE_{nlj} . From equations (4.20) and (4.21) it can be seen that this ratio is equivalent to n_2/n_1 . As expected from equation (4.22), the ratio becomes greater than one around $z_1 = 20$. That is, the choice of level bundling into the specified regions is valid for approximately $z_1 > 20$. This value varies for the different possible j values as can be seen from figures 4.19 - 4.22.

From the C-like superstructure data it was also possible to decide on the critical n values for each bundling region. If one specifies a critical energy difference (ΔE_c) above which bundling is no longer appropriate, n_1 and n_2 can be inferred from equation (4.22). For example using the energy splitting values of the $E_{2P_{3/2}n(l-1/2)}$ and $E_{2P_{3/2}n(l-1/2)J=4}$ levels and a $\Delta E_c = 0.01Ry$ the bundling cut-offs are at $n_1 = 4$ and $n_2 = 15$.

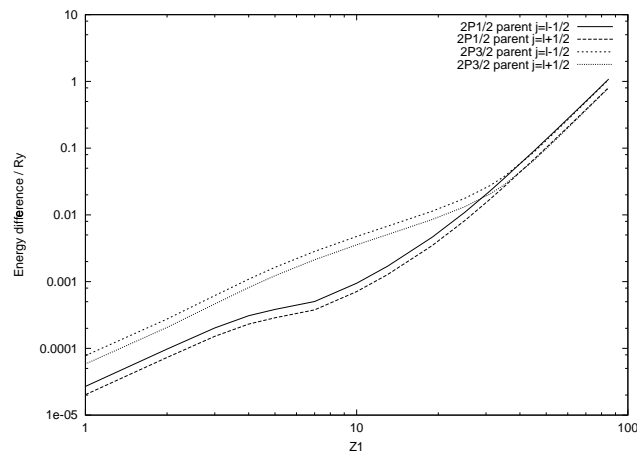


Figure 4.7: E_{nlj} separation from E_{nl} centroid - z_1 dependence. Note that the energy splitting varies as z_1^4 for high z_1 as predicted in equation (4.20). An electronic configuration of $1s^2 2s^2 2p ({}^2P_{1/2}) 5f$ was used throughout the superstructure run.

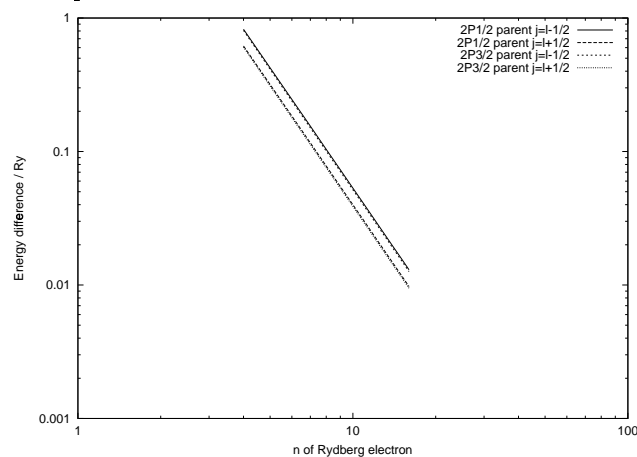


Figure 4.8: E_{nlj} separation from E_{nl} centroid - n dependence. The energy splitting varies as $1/n^3$ as expected from equation (4.20). An l value of 3 for the outer electron was used throughout the n dependence run. z_1 was held constant at 72 to ensure that there was sufficient level splitting at high n to be resolved.

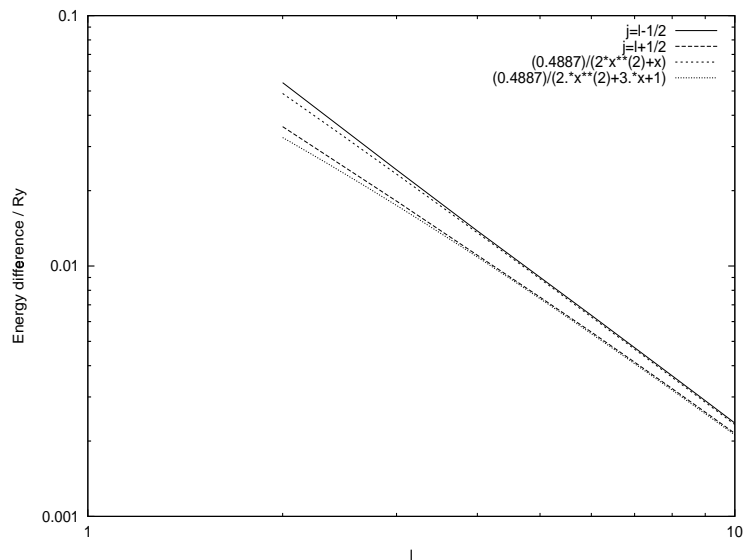


Figure 4.9: E_{nlj} separation from E_{nl} centroid for $^2P_{1/2}$ parent - l dependence. The energy splitting varies exactly as predicted from equation (4.20). An n value of 13 was used for the autostructure run and l varied from 2 through to 10. z_1 was again held constant at 72 to ensure that there was sufficient level splitting to be resolved.

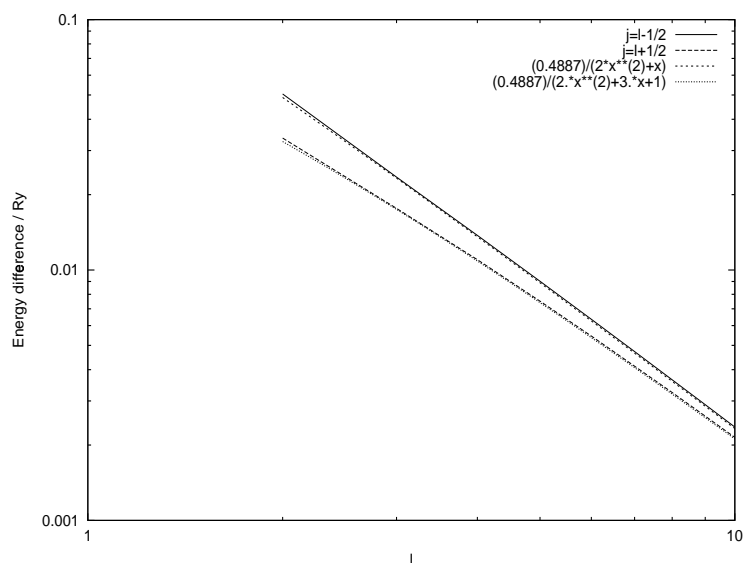


Figure 4.10: E_{nlj} separation from E_{nl} centroid for $^2P_{3/2}$ parent - l dependence. The energy splitting varies exactly as predicted from equation (4.20). An n value of 13 was used for the autostructure run and l varied from 2 through to 10. z_1 was again held constant at 72 to ensure that there was sufficient level splitting to be resolved.

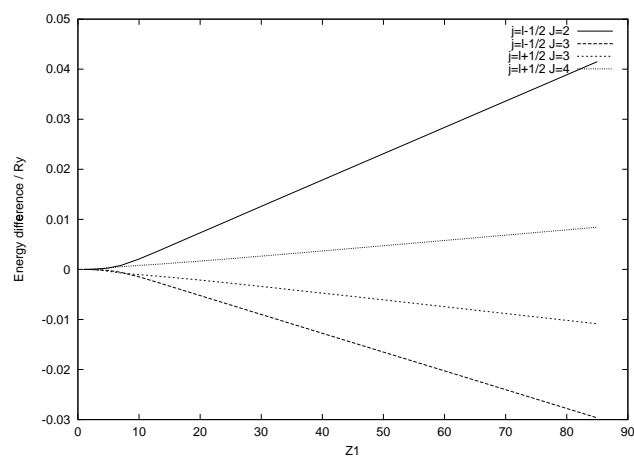


Figure 4.11: E_{nljJ} separation from E_{nlj} centroid for ${}^2P_{1/2}$ parent - z_1 dependence.

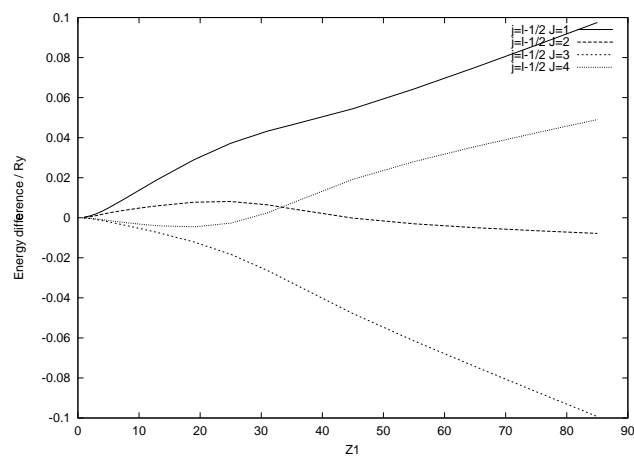


Figure 4.12: E_{nljJ} separation from E_{nlj} centroid for ${}^2P_{3/2}$ parent $j = (l - 1/2)$ - z_1 dependence.

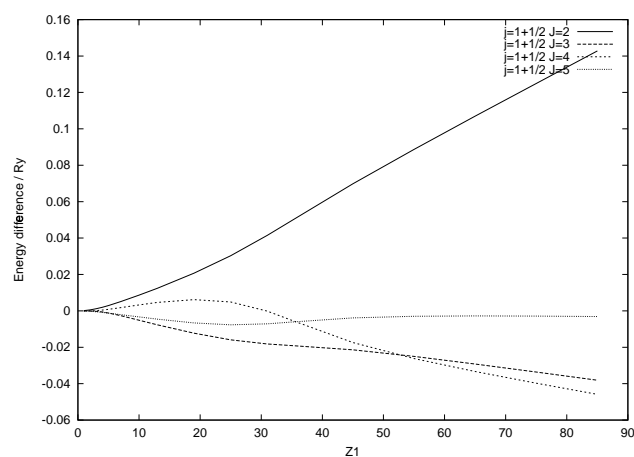


Figure 4.13: E_{nljJ} separation from E_{nlj} centroid for ${}^2P_{3/2}$ parent $j = (l + 1/2)$ - z_1 dependence.

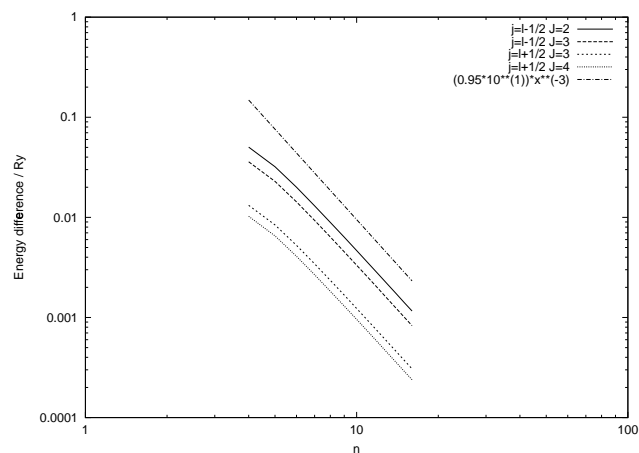


Figure 4.14: E_{nljJ} separation from E_{nlj} centroid for ${}^2P_{1/2}$ parent - n dependence.

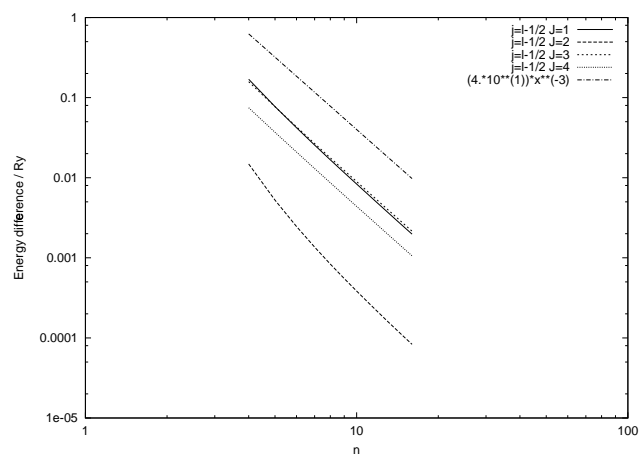


Figure 4.15: E_{nljJ} separation from E_{nlj} centroid for ${}^2P_{3/2}$ parent $j=l-1/2$ state - n dependence.

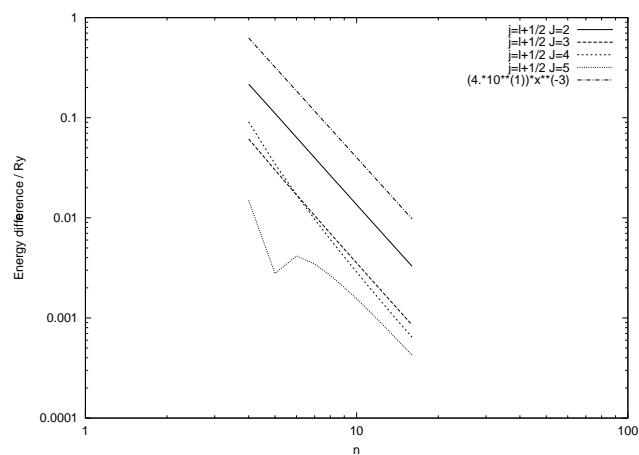


Figure 4.16: E_{nljJ} separation from E_{nlj} centroid for ${}^2P_{3/2}$ parent $j=l+1/2$ state - n dependence.

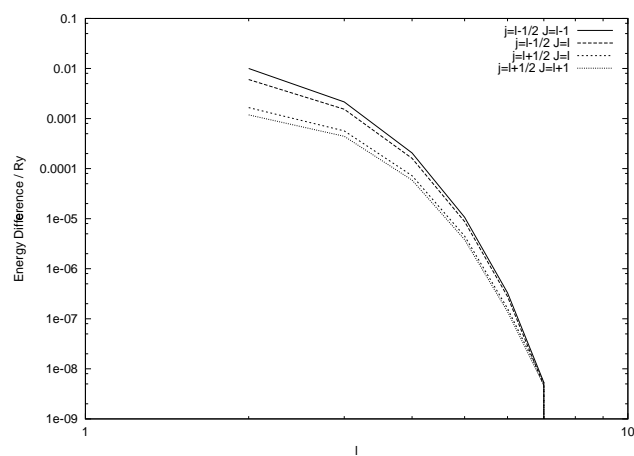


Figure 4.17: E_{nljJ} separation from E_{nlj} centroid for ${}^2P_{1/2}$ parent - l dependence.

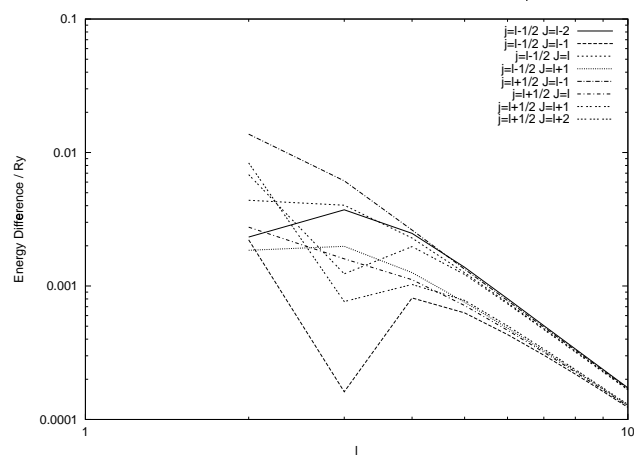


Figure 4.18: E_{nljJ} separation from E_{nlj} centroid for ${}^2P_{3/2}$ parent - l dependence.

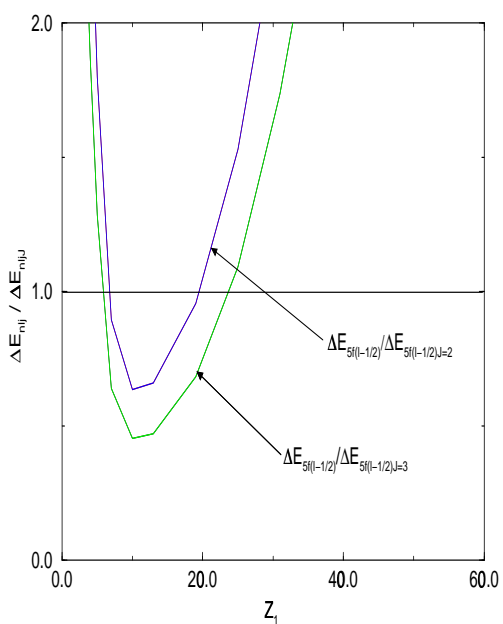


Figure 4.19: $\Delta E_{n_l j} / \Delta E_{n_l j}$ for ${}^2P_{1/2}$ parent, $j=l-1/2$.

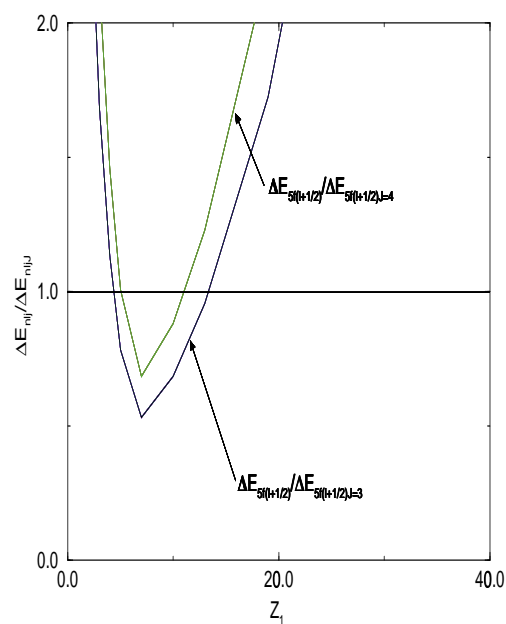


Figure 4.21: $\Delta E_{n_l j} / \Delta E_{n_l j}$ for ${}^2P_{1/2}$ parent, $j=l+1/2$.

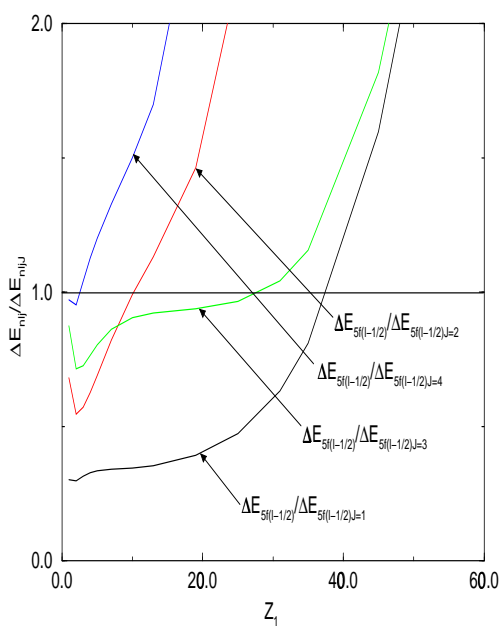


Figure 4.20: $\Delta E_{n_l j} / \Delta E_{n_l j}$ for ${}^2P_{3/2}$ parent, $j=l-1/2$.

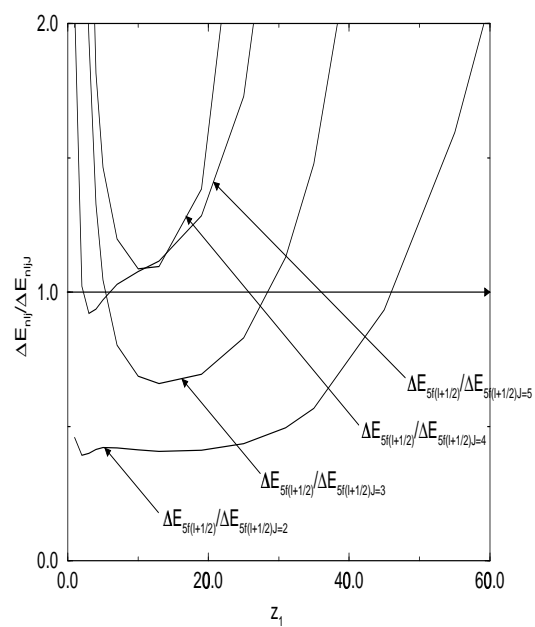


Figure 4.22: $\Delta E_{n_l j} / \Delta E_{n_l j}$ for ${}^2P_{3/2}$ parent, $j=l+1/2$.

4.4.2 Collisional redistribution evaluated

It has been seen that the energy splitting of a given atomic system can be predicted. Of course the actual source of the levels becoming statistically populated (with respect to each other) is that ion collisions redistribute the electrons within a given set of levels faster than they can decay through spontaneous emission. These ion collisions are strongly dependent upon the energy level splitting, and thus it is important to be able to track the splitting for any system being investigated, as in the previous section. To ensure that the levels are statistically populated one must look at the actual collisional rates. There are two main collisional rates that can redistribute the electrons amongst the J levels of a given $(J_P)nlj$ group that must be considered for the n_1 cut-off to be diagnosed. The first process is collisionally induced quadrupole transitions between members of the $(J_P)nlj$ group, and the second is dipole transitions from adjacent l states.

Quadrupole transitions within the one $(J_P)nlj$ group

Consider a set of J levels within a given parent and j . The critical density at which the J -levels will be relatively statistically populated will be given by

$$N_{c_1}^{(zeff)} = \langle A_J \rangle / \langle\langle q_{J \rightarrow J'}^{(zeff)} (T^{(zeff)}) \rangle\rangle \quad (4.23)$$

where $\langle A_J \rangle$ denotes the average over J of the level reciprocal radiative lifetime and $\langle\langle q_{J \rightarrow J'}^{(zeff)} \rangle\rangle$ denotes the rate coefficient summed over final states J' and averaged over initial states J . Note that this is for transitions between J populations of the same $(J_P)nlj$ group.

It was possible to evaluate the ion collisional redistribution rate using a code based on the theory given in Alder et al. (1956). The code was taken from the ADAS database of codes at JET and was originally developed by Summers. The code was originally designed to model proton collisional rates for any given target. It was possible to scale the proton collisional cross sections to apply to any colliding ion. This is shown briefly below.

Cross section scaling for heavy ions

The proton collisional cross sections scale in a straightforward manner to the cross sections for ion collisions. The ion collisional rate, $q(T_i)$, is found from the cross section $\sigma_i(v)$. Assuming a Maxwellian velocity distribution for the colliding ions $q(T_i)$ is given by

$$\begin{aligned} q(t_i) &= \int_0^\infty 4\pi \left(\frac{m_i}{2\pi kT_i} \right)^{3/2} v^2 e^{-\frac{mv^2}{2kT_i}} v \sigma_i(v) dv \\ &= \int_{E_0}^\infty 8\pi \left(\frac{m_i}{2\pi kT_i} \right)^{3/2} \frac{1}{2} m_i v^2 m_i^{-\frac{1}{2}} \sigma_i(v) dE \end{aligned} \quad (4.24)$$

The ion collisional cross sections are equal to z_i^2 (the effective charge of the collider) times the proton collisional cross section evaluated at the same velocity. That is if E_p is the proton energy and E_i is the ion energy, then

$$\begin{aligned} E_i &= \frac{1}{2} m_i v^2 \\ &= \frac{1}{2} m_i \frac{E_p}{\frac{1}{2} m_p} \\ &= \frac{m_i}{m_p} E_p \end{aligned} \quad (4.25)$$

Thus

$$\sigma_i(E_i) \rightarrow z_i^2 \sigma_p(E_p) \quad (4.26)$$

Therefore

$$\begin{aligned} q(T_i) &= \int_{E_0}^\infty \frac{8\pi}{m_i^{\frac{1}{2}}} \left(\frac{1}{2\pi kT_i} \right)^{3/2} E_i e^{-\frac{E_i}{kT_i}} z_i^2 \sigma_p(E_p) dE_i \\ &= \int_{E_0}^\infty \frac{8\pi}{m_i^{\frac{1}{2}}} \left(\frac{1}{2\pi kT_i} \right)^{3/2} \frac{m_i}{m_p} E_p e^{-\frac{m_i}{m_p} \frac{E_p}{kT_i}} z_i^2 \sigma_p(E_p) \frac{m_i}{m_p} dE_p \\ &= \int_{E_0}^\infty \frac{8\pi}{m_p^{\frac{1}{2}}} \left(\frac{1}{2\pi k \left(\frac{m_p}{m_i} T_i \right)} \right)^{3/2} E_p e^{-\frac{E_p}{k \left(\frac{m_p}{m_i} T_i \right)}} z_i^2 \sigma_p(E_p) dE_p \\ &= z_i^2 q_p(T_p) \end{aligned} \quad (4.27)$$

where

$$T_p = \frac{m_p}{m_i} T_i \quad (4.28)$$

is the scaled proton temperature. Thus in order to run the code for any possible collider, one has to evaluate the proton temperature at this scaled temperature and multiply the cross section by z_i^2 .

The C-like sequence was used to illustrate the behaviour of $N_{c_1}^{(zeff)}$ for the electric quadrupole transitions. The superstructure code (Eissner et al., 1974) was run to generate the fundamental atomic data required to evaluate these rates. The system was restricted to two allowed configurations, namely

- $1s^2 2s^2 2p^2$
- $1s^2 2s^2 2p : nd$

where nd represents the Rydberg electron that could be placed in a range of n-shells. The possible J-values that the system can take are shown in table 4.4.2.

Configuration	Parent	j	possible J
$1s^2 2s^2 2p^2$	$^2P_{1/2}$	3/2	2,1
$1s^2 2s^2 2p^2$	$^2P_{1/2}$	1/2	1,0
$1s^2 2s^2 2p^2$	$^2P_{3/2}$	3/2	3,2,1,0
$1s^2 2s^2 2p^2$	$^2P_{3/2}$	1/2	2,1
$1s^2 2s^2 2p : nd$	$^2P_{1/2}$	5/2	3,2
$1s^2 2s^2 2p : nd$	$^2P_{1/2}$	3/2	2,1
$1s^2 2s^2 2p : nd$	$^2P_{3/2}$	3/2	3,2,1,0
$1s^2 2s^2 2p : nd$	$^2P_{3/2}$	5/2	4,3,2,1

For the purposes of evaluating the ion collisional rates, it was decided to look at the $1s^2 2s^2 2p(^2P_{3/2}), j = l - 1/2$ set of levels to see at which point the ion collisions balance the spontaneous emission rate. With the configuration chosen it is possible to get electric quadrupole transitions between the J levels of this group and dipole allowed spontaneous emission to any of the ground configuration terms allowed for within the

$\Delta J \leq 1$ selection rule (as there will always be a change of parity between the Rydberg electron configuration and the ground). For the highly excited electrons, there will also exist many other spontaneous emission decay routes that are not accounted for within the simple atomic structure chosen for the superstructure runs. Thus it was decided to evaluate hydrogenic A-values for each $1s^2 2s^2 2p : nd$ set of levels. In this way a more accurate lifetime could be calculated for use in equation (4.23).

The ion collision code needs to know the energy values, electric quadrupole line strengths and the statistical weights for each level involved in the transition as well as the effective charge of the projectile and ion temperature of the plasma. The superstructure code was run to get the energy level values and the electric quadrupole line strengths. This was done for a range of n-shells, z_1 's and ion temperatures. Alpha particles were used as the colliders to illustrate the results in the context of a fusion tokamak.

To evaluate equation (4.23) it was then necessary to form the various averages. $\langle A_J \rangle$ was calculated by finding the average over J of the total spontaneous emission rates from each level. Similarly $\langle\langle q_{J \rightarrow J'}^{(z_{eff})}(T^{(z_{eff})}) \rangle\rangle$ was found by taking the average over J of the total ion collisional rate (excitation and de-excitation) from each J to all the other possible J levels in the $j=l-1/2$ set of levels. The results are shown in figures 4.23 - 4.26.

It can be seen that the average A-values increase with z_1 and falls off with increasing n . This is as expected due to the excited electron being held closer to the core for high z_1 , thus allowing for stronger decay to the lower states. Similarly for higher n , the electrons are further from the core and so less likely to decay.

Note that the critical density scaling is as expected with $N_{c_1}^{(z_{eff})}$ increasing with z_1 and decreasing as one progresses up the various n-shells. It can also be seen that for a light element of $z_1 \approx 1$ and $n \approx 15$, the critical density for statistical redistribution in J occurs at a reasonable value ($N_{c_1} \approx 1 \times 10^{10} cm^{-3}$).

In order to evaluate the critical n-shell above which the levels are statistically populated we plot $\langle A_J \rangle / (\langle\langle q_{J \rightarrow J'}^{(z_{eff})}(T^{(z_{eff})}) \rangle\rangle N_{ion})$, see figure 4.27 for the results. The critical n-shell is the one at which the curves cross 1. The plot shows the results for a range of effective nuclear charges. The results are as one would expect, with

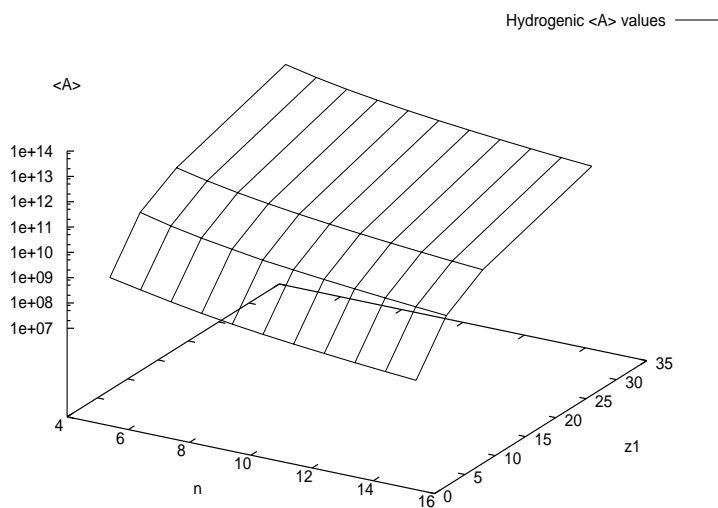


Figure 4.23: A-values for the range of physical parameters that the autostructure code was run, n and z_1 dependence.

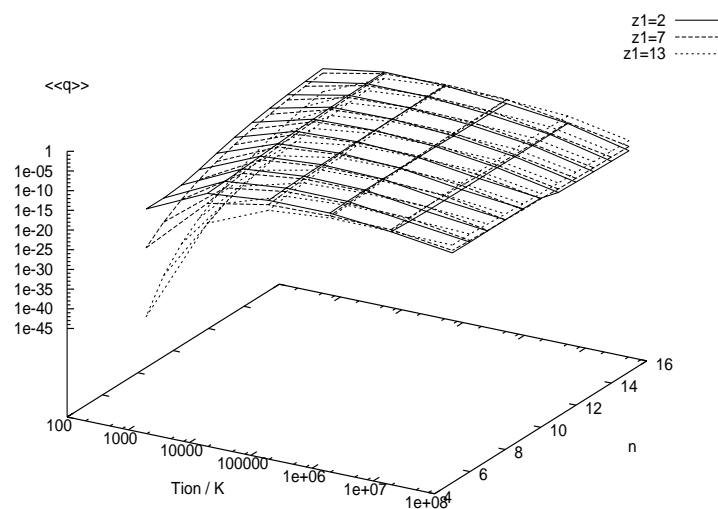


Figure 4.24: Ion quadrupole collisional rates as a function of temperature and n-shell.

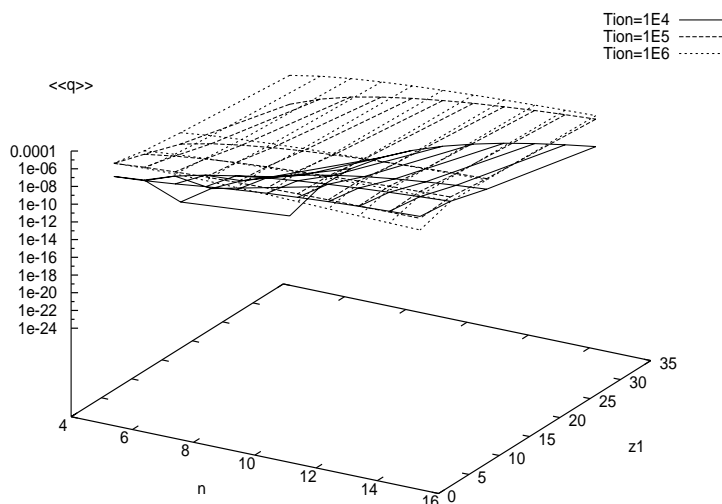


Figure 4.25: Ion quadrupole collisional rates as a function of n-shell and z_1 .

$n \approx 9$ for $z_1 = 2$ and $n \approx 15$ for $z_1 = 7$.

Dipole allowed transitions between adjacent l states

There is a second mechanism of indirect J redistribution by transfer from $nljJ$ to $nl \pm 1j'J'$. Note that because of the near degeneracy in the relativistic picture of $nl_{l+1/2}$ and $nl + 1_{l-1/2}$, it is only the collisional rates between $nl_{l+1/2}J$ and $nl + 1_{l-1/2}J'$ which matter. These are allowed dipole transitions but again induced by positive ion impact. The critical density for redistribution by this pathway is

$$N_{c_1}^{(zeff)} = \langle A_J \rangle / \langle\langle q_{nlJ \rightarrow nl \pm 1J'}^{(zeff)}(T^{(zeff)}) \rangle\rangle \quad (4.29)$$

The critical density for J redistribution is the smaller of the N_{c_1} values from equations (4.23) and (4.29). Alternatively, for specified $N^{(zeff)}$ in the plasma, we seek the lowest value of n ($= n_1$) for $l > 1$ for which the equalities are acceptably satisfied.

Transitions from $nljJ$ to $nl \pm 1j'J'$ levels were evaluated for the C-like sequence to illustrate the critical density and n-shell behaviour. For the rates, the same code

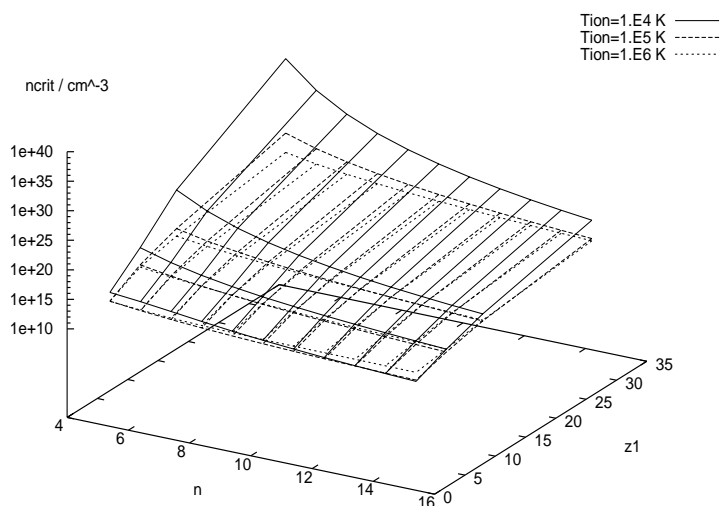


Figure 4.26: Critical density at which the ion quadrupole collisions balance the spontaneous emission rates from the $j=l-1/2$ set of levels.

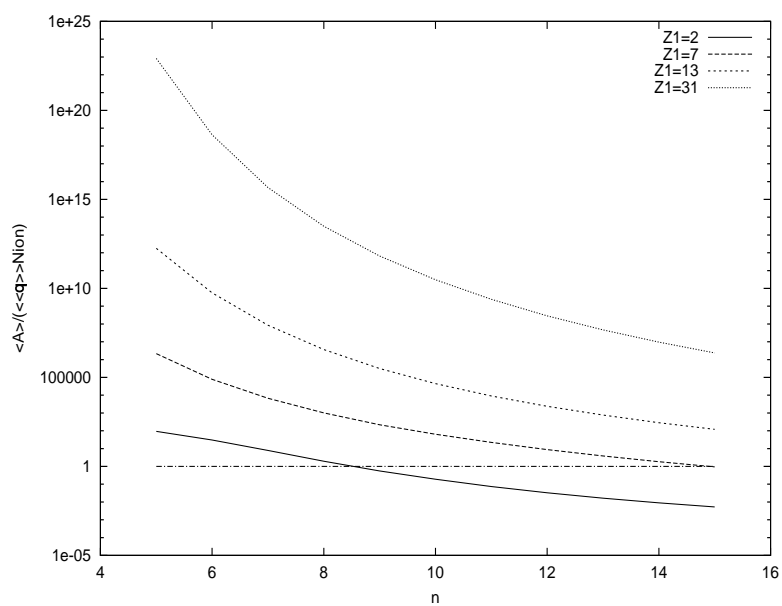


Figure 4.27: Critical n-shell plot showing the critical value at which the ion collisions balance the spontaneous emission rates from the $j=l-1/2$ set of levels. A collider density of $1 \times 10^{14} \text{ cm}^{-3}$ and temperature of $1 \times 10^4 \text{ K}$ were used.

as that for the nlj test code was used. The superstructure code was again run to generate the atomic data necessary for the code. An atomic structure of $1s^22s^22p : nl$ was used, this time the Rydberg electron was allowed to occupy either the p, d or f states and make transitions between them or alternatively down to the ground $1s^22s^22p^2$ configuration. Results were generated for a range of n-shells and nuclear charges.

The Pengelly/Seaton code requires energy level values, absorption oscillator strengths, statistical weights, all of which were extracted from the superstructure runs. The code also requires initial and final state lifetimes. Due to the simple atomic structure used in the superstructure runs, there were many spontaneous decay routes which were not accounted for. To allow for realistic lifetimes to be produced, hydrogenic A-values were again generated for each level of interest, accounting for decay to all possible lower states. In this way the $nd \ ^2P_{1/2}$ set of levels were investigated, considering all the possible dipole collisional transitions to and from the adjacent l states, and spontaneous decay to all allowed lower states.

The $\langle A_J \rangle$ and $\langle\langle q \rangle\rangle$ values are shown in figures 4.28 and 4.29, and both scale as one would expect. The critical density at which statistical redistribution occurs was plotted for a range of n and z_1 values, see figure 4.30. As can be seen, there is a straightforward increase of the critical density with z_1 , and a decrease with n . There is also a slight increase with collider temperature, with the ion collisions becoming less effective at higher temperatures. The critical n-shell at which redistribution occurs was also plotted for a range of z_1 's, see figure 4.31. As before, the results are intuitive and verify the proposed bundling method with statistical redistribution occurring at $n \approx 5$ for $z_1 = 2$ and $n \approx 12$ for $z_1 = 7$.

Thus one can see that it is possible in principal to evaluate the n_1 cut-off for any medium/heavy element.

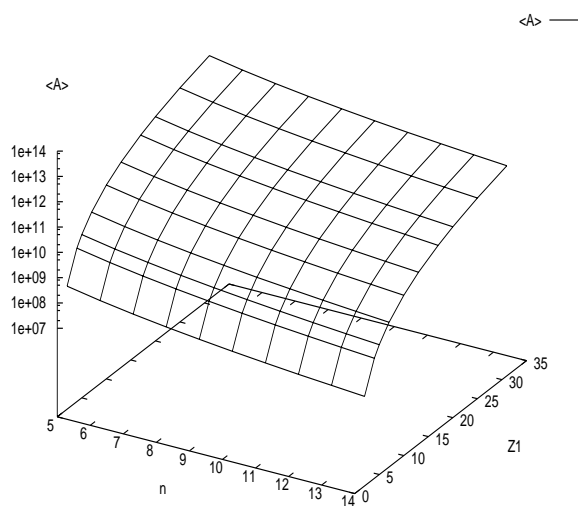


Figure 4.28: $\langle A_J \rangle$ evaluated for the C-like system for the $1s^2 2s^2 2p : nd$ set of levels.

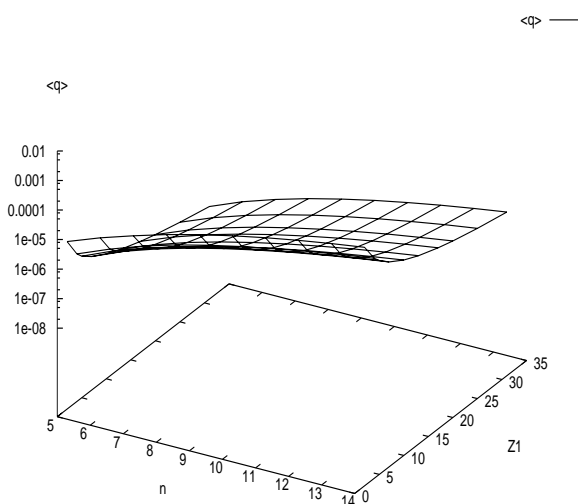


Figure 4.29: $\langle\langle q_{nlJ \rightarrow nl \pm 1J'}^{(z\text{eff})}(T^{(z\text{eff})}) \rangle\rangle$ evaluated for the C-like system for the $1s^2 2s^2 2p : nd$ set of levels for a collider temperature of $1 \times 10^4 K$.

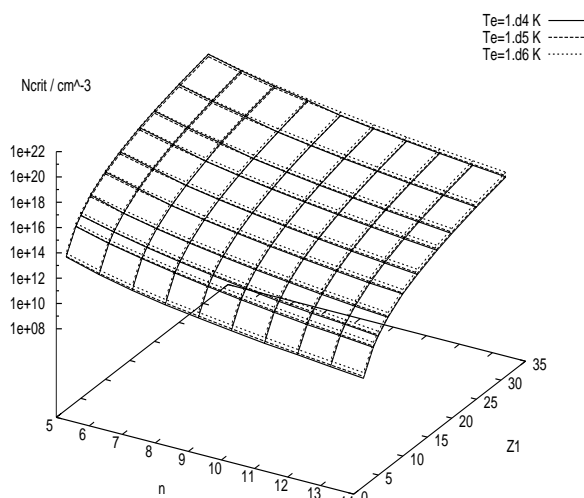


Figure 4.30: $\langle A_J \rangle / (\langle \langle q_{nlJ \rightarrow nl \pm 1J'}^{(z\text{eff})}(T^{(z\text{eff})}) \rangle \rangle)$ evaluated for the C-like system for the $1s^2 2s^2 2p : nd$ set of levels.

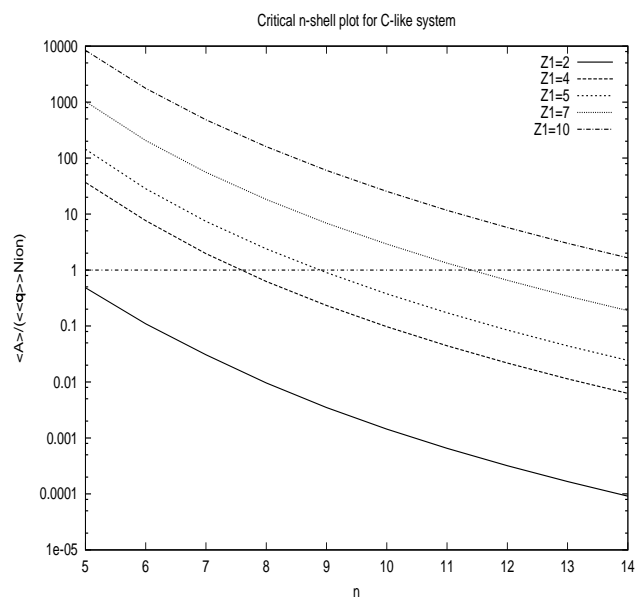


Figure 4.31: $\langle A_J \rangle / (\langle \langle q_{J \rightarrow J'}^{(z\text{eff})}(T^{(z\text{eff})}) \rangle \rangle N_{ion})$ evaluated for the C-like system for the $1s^2 2s^2 2p : nd$ set of levels. A collider density of $1 \times 10^{14} \text{ cm}^{-3}$ and temperature of $1 \times 10^4 \text{ K}$ were used for all the results shown.

4.5 Conclusions

In this chapter much of the ground work for the new collisional-radiative code for application to heavy elements has been laid down. The new bundling scheme has been described and a code developed for the bundled-nl and bundled-n block primitives. A test module to evaluate the bundled-nlj block primitives has been demonstrated, and the usefulness of this approach in the development of future modules is clear. The necessary Gaunt factors for the new code have been developed and an investigation into the automation of detection of the bundling cut-offs performed using standard ion collisional rate expressions.

The thesis work presented here is a stepping stone into the full development of the new heavy species code. The lower levels will be dealt with in the existing ADAS 208 approach, requiring a phase of intensive fundamental atomic data production for the heavy species to be investigated. A code has to be developed to evaluate the new j-j coupled and cross-coupled Gaunt factors. Also, the bundling cut-off scheme has to be fully automated. This work is planned for the next phase of the ADAS collisional-radiative development. For a more indepth discussion on the future work necessary to carry the work here through to completion see chapter 6.